

Shake and Take: Fast Transformation of an Origami Gripper

Chang Liu^{ID}, Samuel J. Wohlever^{ID}, Maria B. Ou, Taskin Padir^{ID}, and Samuel M. Felton^{ID}

Abstract—Origami structures can transform their form and function by changing the direction of their folds. This reconfiguration can enable multifunctional robots, but doing so requires a fast, robust, and repeatable actuation method. In this article, we present an origami gripper that uses dynamic transformation to change its kinematic behavior in less than a second. We characterize individual vertices to show that the transformation is predictable and repeatable for different designs and orientations. We then apply it to a multivertex template that is capable of a wide range of shapes and motion patterns, indicating that transformation can be generalized to complex and functional machines. To demonstrate this, we built a transforming origami gripper on a robotic arm to pick up multiple objects. Demonstrations show that the gripper can quickly reconfigure between three different grasping modes and has sufficient stiffness to engage with and lift multiple objects with distinct geometries.

Index Terms—Dynamics, gripper design, mechanism design, origami, origami robots, reconfigurable robots, robotic grasping, transformation.

I. INTRODUCTION

ORIGAMI-INSPIRED engineering has appeared in a variety of applications, including micromanufacturing [1], [2], antennas [3], [4], space deployment [5]–[7], and robotics [8]–[10]. One particularly exciting application is transforming robots, in which a machine changes its shape and kinematic behavior by changing the way its creases are folded. There are many examples of machines that transform from “flat” to “functional” configurations [11], [12] and others that switch between multiple 3-D shapes [13], [14].

This transformation can be driven by a variety of actuation techniques. Self-folding describes a large range of low-profile torsional actuators embedded on the creases of an origami

Manuscript received October 20, 2020; revised February 20, 2021; accepted April 16, 2021. This article was recommended for publication by Associate Editor R. Ozawa and Editor P. Dupont upon evaluation of the reviewers’ comments. This work was supported by Northeastern University. (*Corresponding author:* Samuel M. Felton.)

Chang Liu is with the Department of Electrical and Computer Engineering, University of California, Los Angeles, CA 90095 USA (e-mail: changliu498@ucla.edu).

Samuel J. Wohlever and Maria B. Ou are with the Department of Mechanical and Industrial Engineering, Northeastern University, Boston, MA 02115 USA (e-mail: wohlever.s@northeastern.edu; ou.m@northeastern.edu).

Taskin Padir and Samuel M. Felton are with the Institute for Experimental Robotics, Northeastern University, Boston, MA 02115 USA (e-mail: t.padir@northeastern.edu; smfelton@gmail.com).

This article has supplementary material provided by the authors and color versions of one or more figures available at <https://doi.org/10.1109/TRO.2021.3076563>.

Digital Object Identifier 10.1109/TRO.2021.3076563

structure to induce folding [15]. Self-folding has been demonstrated with hydrogels [16]–[18], shape memory materials [19], [20], magnets [14], [21], and many other phenomena. Other origami machines have used different actuation techniques, including cables routed through an origami arm [22], spring-loaded wings [23], and centrifugal forces [24].

Unfortunately, many physical examples of origami transformation cannot perform useful tasks. In some, the actuation time is too slow for real-world applications: while some millimeter-scale devices can fold in just seconds [25], machines larger than a few centimeters can take anywhere from 40 s [22] to minutes [26] or even hours [18] to complete their transformation. Other methods are not energy efficient. The first autonomously self-folding robot, for instance, took 8.8 kJ to fold, at an efficiency under 5×10^{-7} [27]. Many self-folding machines are also too compliant to act against their environment—origami machines are inherently slender and their low-profile actuators exert minimal torque, limiting overall mass. For example, pneumatic self-folding grippers were only able to hold paper objects [28], and hinges actuated by shape memory polymers could only fold faces under 20 cm long against gravity [29].

Finally, origami mechanisms are prone to “misfolding”—folding one or more creases in the wrong direction—making transformation risky. The flat state of an origami mechanism is a kinematic singularity, so even constrained mechanisms can become uncontrollable when flat [30]. Because origami transformation requires some or all of the creases to pass through the flat state, the process is susceptible to misfolding [31], [32], and this risk is exacerbated when combined with the compliance and slow speeds mentioned earlier.

In contrast, dynamic origami transformation [33] is a relatively new approach that is both fast and reliable. This transformation can be described conceptually by considering each vertex in the origami pattern as a bistable mechanism. Kinematically, the origami pattern is constrained, but if it is excited dynamically, the inertia of the facets causes the mechanism to deform. If the mechanism deforms far enough, some of the creases may snap through the unstable equilibrium point and change their fold direction. This changes the kinematic relationship between the creases and “transforms” the overall mechanism. Previous studies have shown that this transformation can be actuated with a single electric motor [33], [34] or spring-loaded cell [35] and can occur in less than a second for structures up to 35 cm in length.

While this method is faster and more reliable than previous self-folding actuators, it has its own limitations. Because

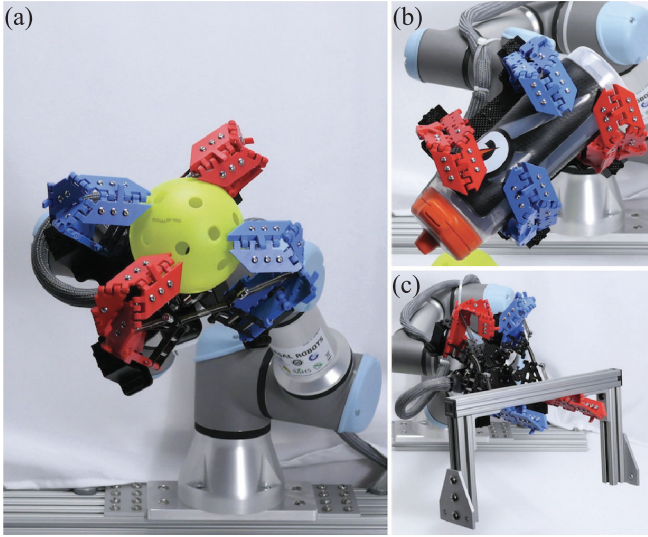


Fig. 1. Dynamically reconfigurable origami gripper that can perform three different grasps by transforming the kinematics of its fingers. These grasps include (a) a radial pinch, (b) a cylindrical wrap, and (c) a forklift-style lift for high loads.

transformation required a relatively low stiffness, previous implementations were too compliant to be functional. To address this issue, we developed a new mechanical template for origami vertices that has a nonlinear stiffness profile. Each hinge exhibits backlash—some nontrivial displacement with zero stiffness. Within the backlash range, transformation requires minimal energy. Furthermore, the backlash of each vertex can be altered by folding or unfolding the mechanism. Effectively, we can “turn OFF” transformation by folding the mechanism and “turn it ON” by unfolding it to a near-flat state.

To demonstrate the efficacy of this concept, we first characterized individual vertices that are the building blocks of our origami systems. We measured their stiffness and transformation properties under a variety of orientations to understand how they would behave in realistic applications. We then applied this transformation to a multivertex template known as an origami string [36]. These strings are kinematically capable of tracing any path in 3-D space [37] and can exhibit a wide range of motion patterns, so demonstrating transformation in these strings shows that transformation can be generalized to many different machines. Finally, we constructed a robotic gripper with four origami fingers that could transform between three different grasp modes through dynamic excitation (see Fig. 1). We demonstrated that this gripper could grab multiple objects with different grasps and reliably transform between those grasps in less than a second.

II. VERTEX DESIGN AND FABRICATION

A. Vertex Design

The mechanisms in this article are based on the origami string [36], [37]. The base element of this string is the Miura vertex [see Fig. 2(a)]. This vertex comprises four creases: two collinear spinal creases and two peripheral creases offset from

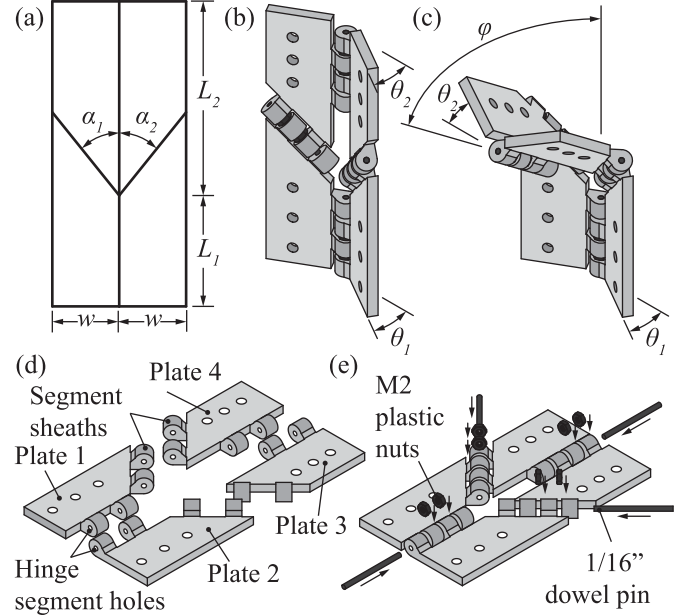


Fig. 2. Vertex design and fabrication. (a) Crease pattern. (b) Parallel configuration. (c) Antiparallel configuration. (d) Plates are 3-D printed. (e) M2 plastic nuts are inserted between segment sheaths. Pins are inserted along the hinges to align the plates.

the spine by angles α_1 and α_2 . It has a single degree of freedom. We consider the fold angle of the lower spinal crease θ_1 to be the input and the upper spinal crease θ_2 to be an output. Each Miura vertex has two configurations: the parallel configuration is when central spinal creases are collinear and the peripheral creases are flat [see Fig. 2(b)], and the antiparallel configuration is when central spinal creases are offset by an angle φ_a and the peripheral creases have a nonzero fold angle [see Fig. 2(c)]. The kinematic relationships between these angles can be found in previous publications [14], [33], [36], [38]. In either configuration, the magnitude of the spinal angles is equal, so $|\theta_1| = |\theta_2|$. When connected into an origami string, every vertex shares a single spinal line, and every spinal crease along the line has the same fold angle. In this way, when one crease at the base of the string is folded, the entire structure actuates in a constrained manner with a trajectory determined by the fold pattern.

B. Vertex Fabrication

We printed facets as individual pieces with a Prusa i3 MK3s using polylactic acid plastic. Each plate included segmented sheaths along the crease edges [see Fig. 2(d)] to house 1/16-in-diameter dowel pins secured with M2 plastic nuts [see Fig. 2(e)]. Creases were assembled by inserting the pins through the interleaved sheaths of the adjacent facets. In contrast to the flexural hinges used in many other origami mechanisms, these hinges have high off-axis stiffness and resistance to deflections outside of the kinematically constrained positions. However, the tolerances in the hinges were made deliberately so that an assembled vertex could deflect slightly beyond its constraints under negligible loads. We refer to this deflection as the backlash φ_b and quantified it by holding one side of the vertex flat and measuring

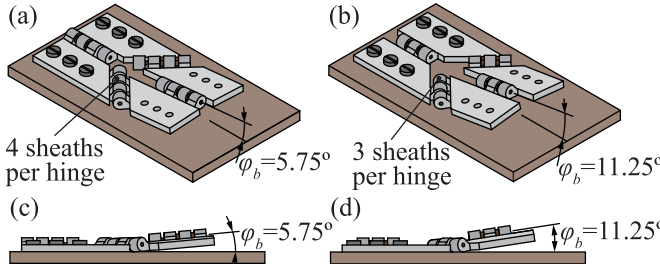


Fig. 3. Backlash φ_b is quantified as the maximum displacement of the upper spinal crease when the lower spinal crease is held flat, without strain in the materials. (a) Small backlash, isometric view. (b) Large backlash, isometric view. (c) Small backlash, side view. (d) Large backlash, side view.

the maximum deflection of the other side under no-load conditions (see Fig. 3). This design makes the vertex stiffness highly nonlinear, with a near-zero-stiffness regime within the backlash range and a high stiffness outside of it.

The vertex samples had the following parameters: $\alpha_1 = \alpha_2 = \alpha = 45^\circ$, $L_1 = 30$ mm, $L_2 = 52.5$ mm, and $w = 22.5$ mm [see Fig. 2(a)]. Holes were put on the faces of plates 1 and 2 [see Fig. 2(d)] to mount the vertex samples to the test base, and the holes on plates 3 and 4 [see Fig. 2(d)] were used to mount extra masses. The barrel hinge holes on plates 1 and 3 were drilled using a 1.58-mm drill bit for a tighter fit, while the hinge holes on plates 2 and 4 were made using a 1.66-mm drill bit for more clearance and backlash. Samples with a smaller backlash ($\varphi_b = 5.75^\circ$) were built with four barrel segments at each hinge [see Fig. 3(a) and (c)] and samples with a larger backlash ($\varphi_b = 11.25^\circ$) had three barrel segments per hinge [see Fig. 3(b) and (d)].

III. VERTEX CHARACTERIZATION

Transformation can be modeled as a comparison between the kinetic energy T of the facets and the transformation energy threshold V_t that must be overcome for the vertex to change its configuration [33]. To validate this model on the new hinge design, we first calculated V_t of individual vertices using their geometry, orientation, and measured stiffness. We then applied a linear displacement to each vertex, calculated T based on its velocity, inertia, and orientation, and observed whether or not transformation occurred.

A. Transformation Energy

The strain in a vertex is minimized when it is in one of the two kinematically constrained states: $\varphi = \varphi_0$ or $\varphi = \varphi_a$. However, it can be deformed into other states and even forced between them. The transformation energy V_t is the amount of energy that must be put into the system at one stable state to overcome the local potential energy maximum and enter the other stable state. To calculate V_t , we first measured the vertex stiffness and used that to calculate the strain energy V_s of the vertex over its displacement φ . We used that curve to identify the local maximum, which is the threshold for transformation. We then calculated the change in gravitational energy V_g between

the stable and threshold states and modeled the transformation energy as the sum of these two components.

1) *Stiffness Measurements*: To characterize the nonlinear stiffness of individual vertices, we measured the stiffness torque τ as a function of displacement φ . We tested two sets of samples: one group had a smaller backlash $\varphi_b = 5.75^\circ$, and the other had a larger backlash $\varphi_b = 11.25^\circ$. The lower segment of each sample was folded to an angle θ_1 and fixed at its base (see Fig. 4). For the smaller backlash, θ_1 was fixed at 5° , 7.5° , 10° , and 12.5° ; for the larger backlash, θ_1 was fixed at 10° , 12.5° , 15° , and 17.5° . We applied a point force F to the tip of the upper spinal crease at a distance L from the vertex with a Mecmesin MultiTest 2.5i and calculated $\tau = F \cdot L$. We measured the displacement of the probe to calculate the deflection of φ between the spinal creases. The probe displaced linearly 50 mm, resulting in a total angular displacement of 40° . The displacement was measured in four sections, alternating the direction of the applied force to avoid snap-through behavior. Each set of parameters was tested three times.

2) *Strain Energy Calculations*: The strain energy $V_s(\varphi)$ is equal to the work done on the vertex for a given deflection φ , so we integrated the stiffness curve $\tau(\varphi)$ to determine V_s along the entire displacement profile

$$V_s(\varphi) = \int_0^\varphi \tau(x) dx. \quad (1)$$

From this curve, we identified the unstable equilibrium point φ_u , where $V_s(\varphi_u)$ is the local maximum between the two stable configurations. The change in strain energy necessary for transformation ΔV_s is the difference between V_s at φ_u and at its starting position φ_0 , which occurs at one of two potential points: $\varphi_0 = 0$ for the parallel starting configuration or $\varphi_0 = \varphi_a$ for the antiparallel starting configuration. For all of the single-vertex experiments, $\alpha_1 = \alpha_2 = \alpha = 45^\circ$

$$\phi_u = \max\{V_s(\varphi) : 0 < \varphi < \varphi_a\} \quad (2)$$

$$\varphi_0 = \begin{cases} 0, & \text{when parallel} \\ 2 \arctan(\sin \theta_1 \tan \alpha), & \text{when antiparallel} \end{cases} \quad (3)$$

$$\Delta V_s = V_s(\varphi_u) - V_s(\varphi_0). \quad (4)$$

3) *Stiffness and Strain Energy Results*: We observed that there was a region of negligible stiffness representing the backlash at two locations on the force-displacement curve; one region was centered at $\varphi = 0^\circ$ and represents the kinematic solution of the parallel configuration, and the other occurred at $\varphi = \varphi_a$, the kinematic solution for the antiparallel configuration. As θ_1 decreased, these regions came closer together until they merged into a single region [see Fig. 5(a) and (c)]. In this region, the vertex can freely transform between the parallel and antiparallel configurations.

In the strain energy plots, the two stable configurations are represented by the local minima, and the peak indicates the energy necessary to transform the vertex from one configuration to the other [see Fig. 5(b) and (d)]. This peak disappears when the fold angle θ_1 is sufficiently small, indicating that transformation will occur with negligible kinetic energy.

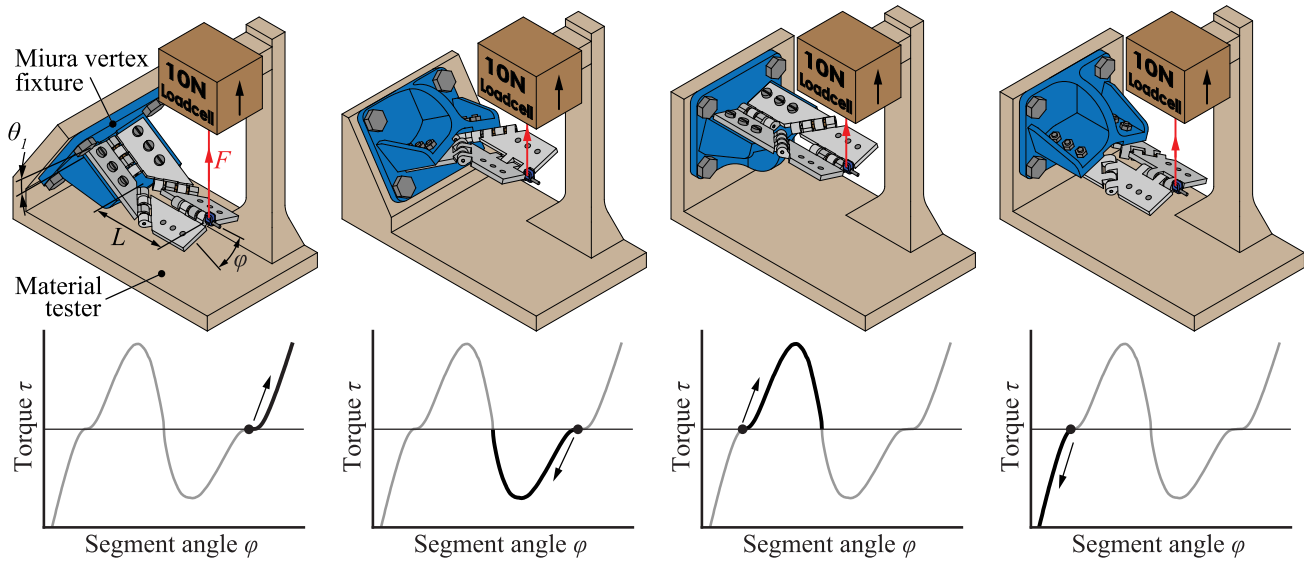


Fig. 4. Stiffness testing rig, with the corresponding section of the torque curve τ being measured. Samples were secured to a fixture with the base segment set at an angle θ_1 . F is the tensile force provided by a load cell, φ is the displacement between the segments, and L is the distance between the vertex and the point where the force is applied.

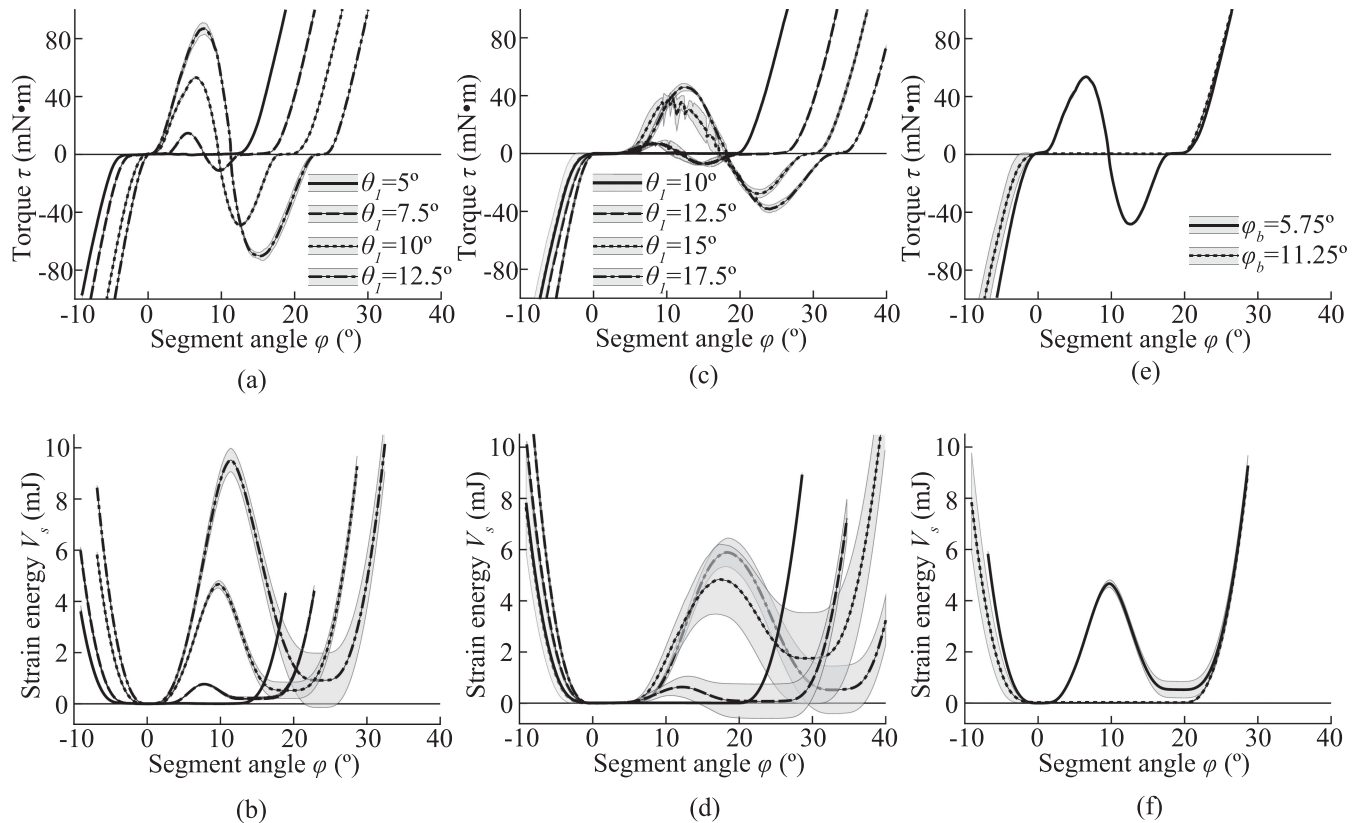


Fig. 5. Stiffness torque τ and strain energy V_s profiles of single vertices over their displacement φ . (a) τ of a vertex with a small backlash and different input angles θ_1 [5° (solid red), 7.5° (solid magenta), 10° (solid blue), and 12.5° (solid black)]. (b) V_s of the same. (c) τ for a vertex with a large backlash and different θ_1 [10° (dashed blue), 12.5° (dashed black), 15° (dashed green), and 17.5° (dashed orange)]. (d) V_s of the same. (e) τ of vertices with a small backlash (solid blue) and large backlash (dashed blue) at $\theta_1 = 10^\circ$. (f) V_s of the same. Shaded areas indicate standard deviation, $N = 3$.

When comparing the stiffness of samples with different backlash values, we see that the size of the backlash region has a substantial effect on the stiffness profile [see Fig. 5(e)] and strain energy peak [see Fig. 5(f)]. At $\theta_1 = 10^\circ$, the small backlash still has a bistable profile, but the large backlash has a single zero-stiffness region with no local maximum.

4) Transformation Energy Calculations: We modeled the transformation energy V_t as the sum of the change in strain energy ΔV_s and change in gravitational energy ΔV_g between the initial position φ_0 and transformation threshold φ_u . The gravitational energy V_g of the vertex is dependent on the weight and orientation of the facets on the distal segment

$$\Delta V_g = V_g(\varphi_u) - V_g(\varphi_0) \quad (5)$$

$$= L_g m g [\sin(\varphi_u - \eta) - \sin(\varphi_0 - \eta)] \quad (6)$$

$$V_t = \Delta V_s + \Delta V_g \quad (7)$$

where m is the upper segment's mass, g is the gravitational acceleration, L_g is the distance between the vertex and the upper segment's center of mass, and η is the tilt angle.

B. Kinetic Energy

The kinetic energy T of the upper segments was calculated from their inertia and the velocity v_s . We measured the velocity of the base v_b with a high-speed camera (Sony Cyber-shot RX100 V, 960 frames/s) and used it to calculate T

$$v_s = v_b \cos \varphi_0 \cos \gamma \quad (8)$$

$$T = \frac{1}{2} m v_s^2 \quad (9)$$

where v_b is the base velocity, m is the mass of the upper segment, and γ is the offset angle.

C. Model Validation

Previous papers posited that (for situations where the input $\theta_1(t) \neq 0^\circ \forall t$) the mechanism transforms if and only if the kinetic energy T of the facets above the vertex is greater than the transformation energy V_t of the vertex [33]. To validate this hypothesis with the new hinge design, we constructed samples with small or large backlashes, fixed their input angle θ_1 , and excited them linearly by accelerating and then stopping them in a direction orthogonal to their base [see Figs. 6 and 7(a) and (b)]. This differs from previous papers [33]–[35], in which kinetic energy came from the input velocity $\dot{\theta}_1$ and corresponding rotation along φ ; these new experiments more closely resemble the motions used to transform the gripper.

We built a testing device [see Fig. 6(a)] that accelerated the vertex in a spring-loaded fixture and then decelerated it with a physical block to approximate an instantaneous stop of the lower segment. The input angle θ_1 of the lower segment was fixed by installing the vertex between a set of plates that were rigidly connected to the accelerating fixture. A high-speed camera was placed above the vertex to measure the velocity of the base [see Fig. 6(b)].

Different velocities were achieved by installing different numbers of springs in the fixture and changing their initial deflection.

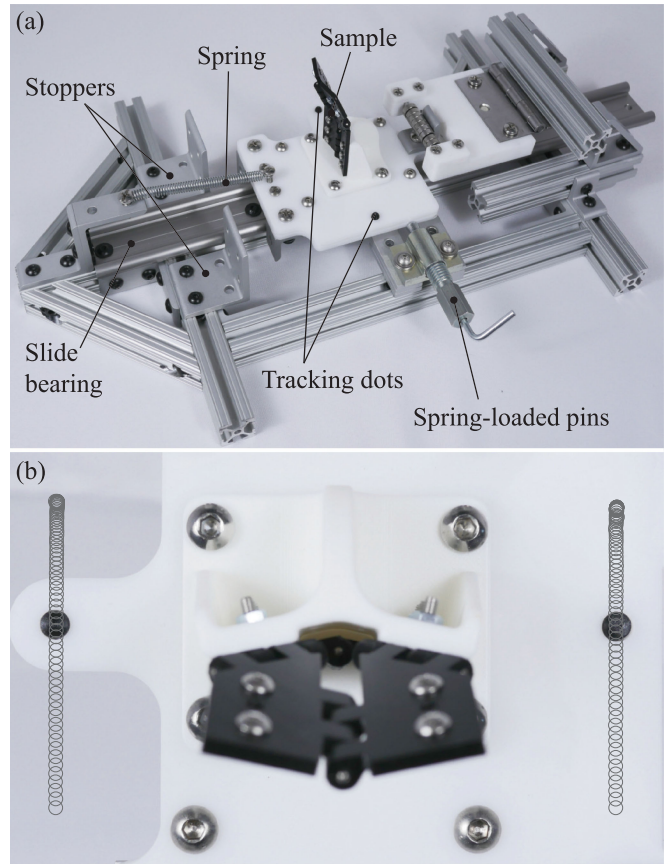


Fig. 6. (a) Dynamic testing fixture used to characterize the vertex dynamics. (b) Top view of the vertex in the fixture. We calculated the translation velocity of the Miura vertex samples by tracking the two black dots on either side.

In some experiments, the facet inertia was modified by adding mass to the upper facets (see Table I). These parameters were chosen so that the kinetic energy of the vertex was slightly less than or greater than the transformation energy, with a difference less than 20%. This was done to test how accurate our model was; by bracketing the expected transformation point with experimental parameters on either side, the experiments would indicate that the model is accurate if we observed transformation when the kinetic energy was slightly greater than the transformation energy, and no transformation when the kinetic energy was slightly less than the transformation energy.

We performed these experiments in a variety of conditions chosen to replicate the orientations we would observe in real-world operations (see Fig. 7). In total, we tested for transformation with 84 different sets of parameters, and each set was tested three times. For each set of parameters, we compared the ratio of the kinetic energy to the transformation energy and observed whether the vertex transformed or not (see Fig. 8). We found that all experiments matched our hypothesis (Dataset S1).

In the first set of experiments, all samples had a backlash $\varphi_b = 5.75^\circ$, with the lower segment oriented vertically and the sample accelerated along the vertex midplane [see Fig. 7(a) and (b)]. The input θ_1 was set to four different values (5° , 7.5° , 10° , and 12.5°), and both initial configurations were tested. For each

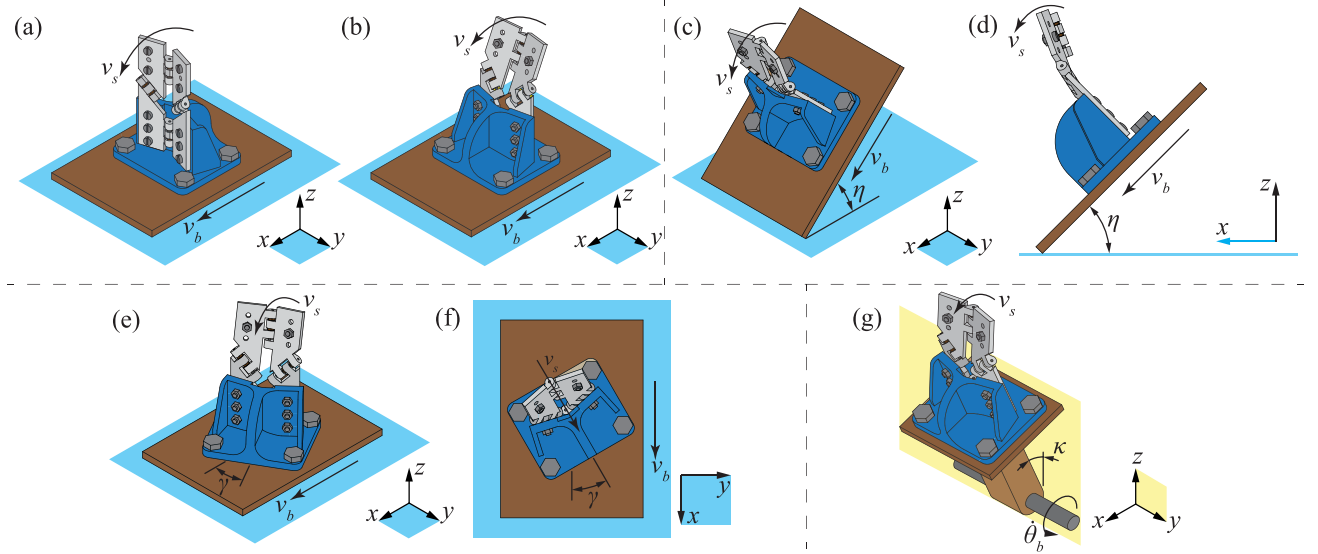


Fig. 7. Dynamic testing cases. Varying backlash, input angle, and initial configuration: (a) an example of large backlash sample with parallel initial configuration and (b) an example of small backlash sample with antiparallel initial configuration. Varying tilt angle η : (c) isometric view and (d) side view. Varying offset angle γ : (e) isometric view and (f) top view. (g) Rotational dynamic testing. κ is the rotational stop angle. V_b is the moving velocity of the base. V_s is the moving velocity of upper two plates. $\dot{\theta}_b$ is the rotational speed.

TABLE I
EXTRA MASS ON VERTICES

Backlash			Small, $\varphi_b = 5.75^\circ$				Large, $\varphi_b = 11.25^\circ$			
Input angle		M3×6 mm screws	5°	7.5°	10°	12.5°	10°	12.5°	15°	17.5°
Number of additional weights	On plate 3	M3 nuts	0	0	1	2	0	0	1	2
	On plate 4	M3×6 mm screws	0	0	1	2	0	0	1	2
Weight of upper two plates (g)		6.4 6.4 8.0 9.6 6.4 6.4 8.0 9.6								

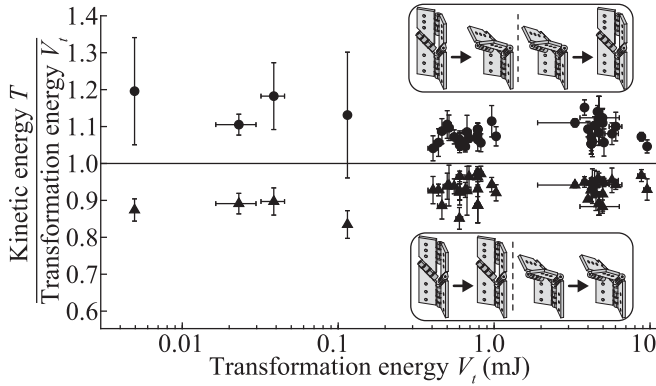


Fig. 8. Ratio of kinetic to transformation energy in attempted transformations of single vertices under 84 different sets of parameters. Circles indicate samples that transformed and triangles indicate samples that did not transform. The line indicates when $T = V_t$, the threshold for transformation. Error bars indicate standard deviation, with sample size $N = 3$.

sample, dynamic testing was run with two velocities selected based on the criteria mentioned above, resulting in 16 total sets of parameters. Results can be seen in Fig. 9(a).

To observe the effect of backlash on transformation, we tested samples with $\varphi_b = 11.25^\circ$. The input θ_1 was set to four different values (10° , 12.5° , 15° , and 17.5°). For each sample, dynamic testing was run with two velocities selected based on the criteria mentioned above, resulting in 16 total sets of parameters. Results can be seen in Fig. 9(b).

To observe the effect of gravity on our model, we tilted the vertices to change the relative direction of gravity on the facets [see Fig. 7(c) and (d)]. In these experiments, all samples had a backlash $\varphi_b = 5.75^\circ$ and were accelerated along the vertex midplane. Samples had a fixed input θ_1 of 7.5° or 10° and one of four different tilt angles η (-90° , -45° , 45° , and 90°) [see Fig. 7(c) and (d)]. For each sample, dynamic testing was run with two velocities selected based on the criteria mentioned above, resulting in 16 total sets of parameters. Results can be seen in Fig. 9(c) and (d).

To test our model under nonorthogonal movements, we accelerated the vertices in a direction offset from the midplane [see Fig. 7(e) and (f)]. All samples had a backlash $\varphi_b = 5.75^\circ$ and were oriented vertically. Samples had a fixed input θ_1 of 7.5° or 10° and were accelerated at an offset angle $\gamma = 45^\circ$ [see Fig. 7(e) and (f)]. For each sample, dynamic testing was run with two velocities selected based on the criteria mentioned above,

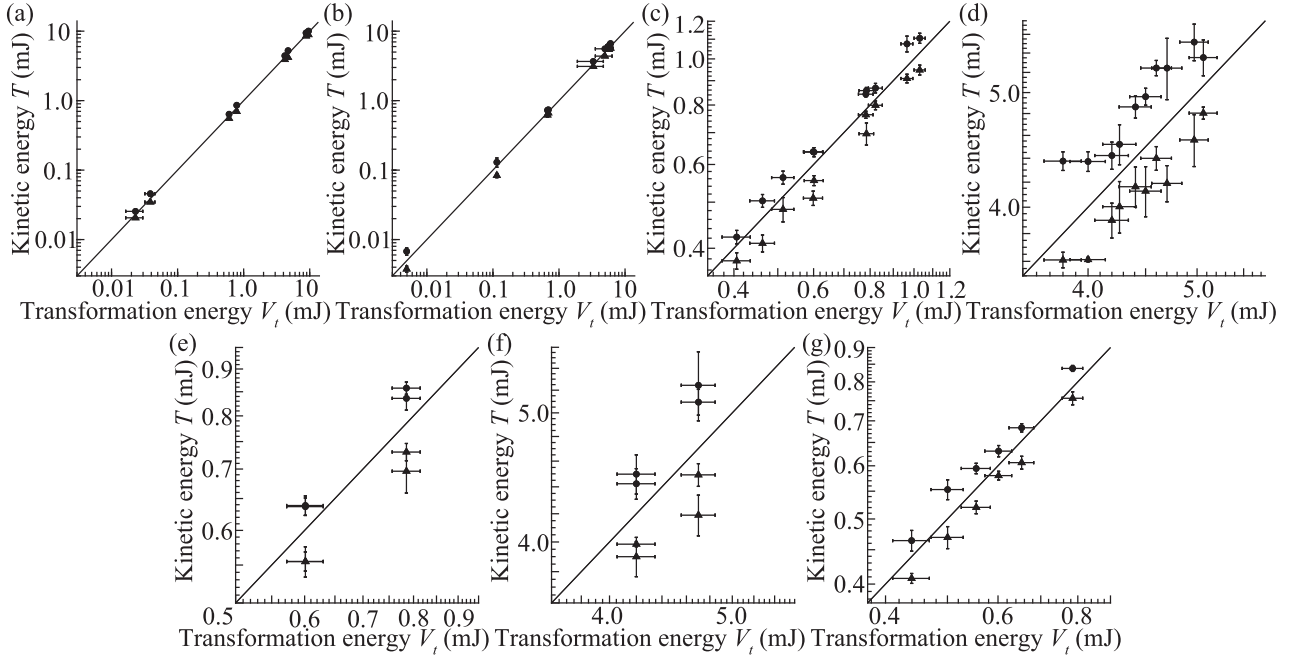


Fig. 9. Kinetic energy T and transformation energy V_t for all dynamic excitation experiments of individual vertices, grouped by parameter. Circles indicate samples that transformed and triangles indicate samples that did not transform. The lines indicate when $T = V_t$, the threshold for transformation. Error bars indicate standard deviation, with sample size $N = 3$. (a) Varying input angle θ_1 for small backlash mechanism, while tilt angle $\eta = 0^\circ$ and offset angle $\gamma = 0^\circ$. (b) Varying input angle θ_1 for large backlash mechanism, while tilt angle $\eta = 0^\circ$ and offset angle $\gamma = 0^\circ$. (c) Varying tilt angle η for small backlash mechanism, while input angle $\theta_1 = 7.5^\circ$ and offset angle $\gamma = 0^\circ$. (d) Varying tilt angle η for small backlash mechanism, while input angle $\theta_1 = 10^\circ$ and offset angle $\gamma = 0^\circ$. (e) Varying offset angle γ for small backlash mechanism, while input angle $\theta_1 = 7.5^\circ$ and tilt angle $\eta = 0^\circ$. (f) Varying offset angle γ for small backlash mechanism, while input angle $\theta_1 = 10^\circ$ and tilt angle $\eta = 0^\circ$. (g) Rotational movement, with input angle $\theta_1 = 7.5^\circ$ and small backlash and stopped at $\kappa = 0^\circ, 30^\circ$, and 60° .

resulting in eight total sets of parameters. Results can be seen in Fig. 9(e) and (f).

To observe the behavior of the vertices under rotation, we installed them in a fixture that rotated the vertices around a point 7.3 cm from their base [see Fig. 7(g)]. All samples had a backlash $\varphi_b = 5.75^\circ$, a fixed input $\theta_1 = 7.5^\circ$, and were accelerated along the midplane. Results can be seen in Fig. 9(g).

In summary, these experiments show that this transformation is robust enough to work under different orientations, and our model remains valid for the different conditions that could occur in a robotic system.

IV. GRIPPER DESIGN AND CHARACTERIZATION

A. Gripper Design

The gripper included four fingers, each of which was an origami string with three vertices [see Fig. 10(a)]. The gripper was capable of performing three different grasps depending on its mode. The pinch mode was designed to grasp objects by applying four radial point forces to an object. It was ideal for picking up smaller objects. The wrap mode was designed to fully encircle an object in one plane, ideal for long thin objects. The forklift mode was designed for larger and heavier objects that could not be enclosed; we demonstrated that the forklift could lift objects up to 11 kg in mass. The complete gripper weighed 650 g, and each finger weighed 45 g. The gripper base was $162.5 \times 180 \times 70$ mm thick, and the fingers were each 190 mm long when straight.

In each mode, the fingers moved along a different trajectory. In the pinch mode, the fingers pinched inward [see Fig. 10(b)]; in the wrap mode, they curled in a spiral [see Fig. 10(c)]; and in the forklift mode, two fingers stayed straight [see Fig. 10(d)], while the other two curled out of the way. Each finger was actuated by an electric motor. When the motor turned, the base of each finger folded or unfolded, causing the finger to close or open in a kinematically constrained trajectory.

The fingers were transformed between the pinch, wrap, and neutral trajectories by reconfiguring their vertices. One way to think about reconfiguration of an origami string is that a vertex is inactive when parallel; the spine remains straight and the string behaves as if the vertex was not there. In contrast, when a vertex is antiparallel, the spine bends and the vertex contributes nontrivially to the string kinematics. In this way, we can design fingers by superimposing two origami strings. When we want the kinematics of one string to be active, we configure the vertices of the other string to be parallel, making them kinematically “invisible.”

To design the fingers’ crease patterns, we first derived α_1 and α_2 from the desired kinematics of each configuration, using geometric models developed in previous work [36]–[39]. This resulted in two vertices for the pinch and two vertices for the wrap; the neutral position did not require any vertices because the string was straight. We found that the distal vertex for both designs was identical, so we combined the two configurations by incorporating three vertices in each finger—the first vertex derived from the wrap kinematics, the second vertex from the pinch

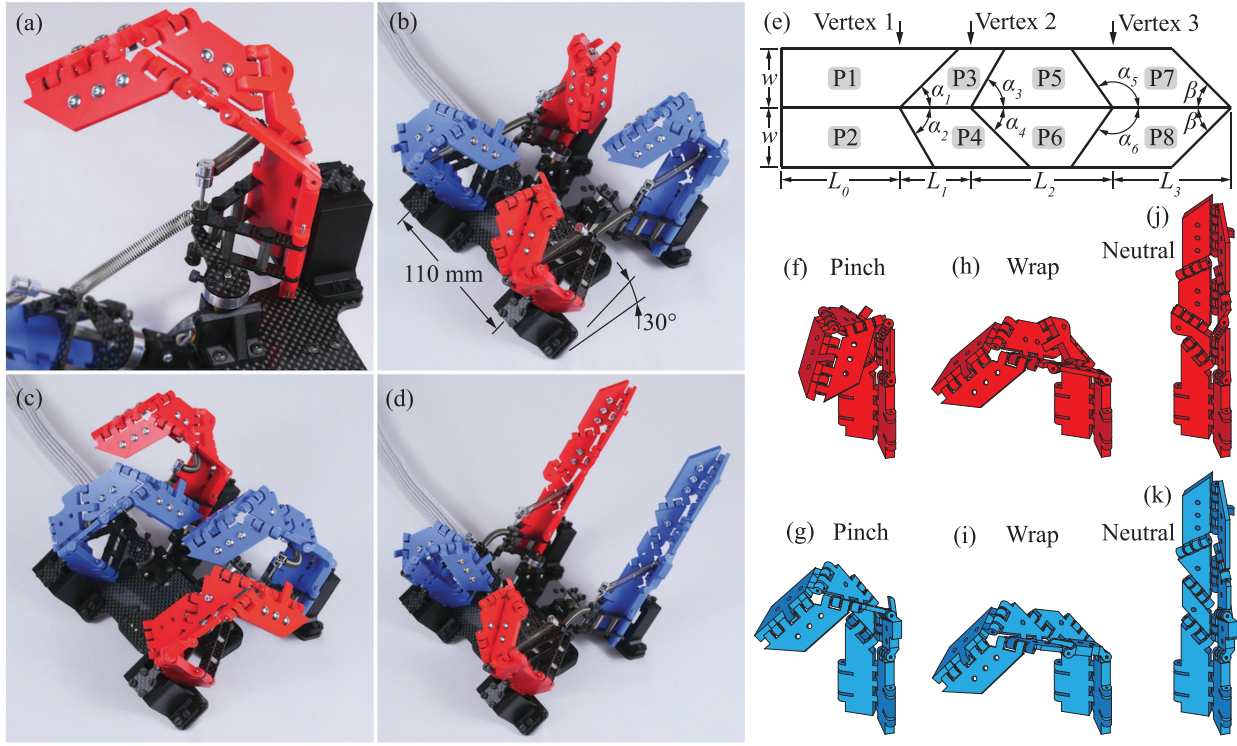


Fig. 10. Gripper design. (a) Finger actuation mechanism. (b) Gripper in radial pinch mode, (c) cylindrical wrap mode, and (d) forklift mode. (e) Origami string template used to design the fingers. w is the width of each plates. L_j is the length of the segment j . α_n are the angles between spinal creases and peripheral creases. β is the fingertip angle. (f) Red finger in a pinch configuration. (g) Blue finger in a pinch configuration. (h) Red finger in a wrap configuration. (i) Blue finger in a wrap configuration. (j) Red finger in a neutral configuration. (k) Blue finger in a neutral configuration.

kinematics, and the third vertex from both kinematic solutions. When the finger needed to perform a wrap, the second vertex was configured to parallel so that it did not affect the kinematics. When the finger was performing a pinch, the first vertex was set to parallel. In summary, the pinch configuration was when the first, second, and third vertices were parallel, antiparallel, and antiparallel, respectively; the wrap configuration was when the vertices were antiparallel, parallel, and antiparallel; and the neutral configuration was when the vertices are all parallel.

The gripper included two finger designs that are differentiated by their color (see Fig. 10), red or blue. Both fingers have similar neutral and wrap kinematics, but their pinching is canted either left (red) or right (blue). The fingers were mounted in a rectangular pattern with same-colored fingers on opposite corners. On each side, a pair of fingers was mounted on an angled plate so that adjacent fingers were 110 mm apart and offset by 30° [see Fig. 10(b)]. The gripper was mounted on a standard UR3e arm. This arm transformed the gripper by flicking the fingers in a controlled manner, causing the vertices to reconfigure between the three possible grasp modes.

After assembly, we characterized the stiffness of each finger to determine the appropriate dynamic input for transformation. We set the input angle θ_1 of the finger to 12.5° and measured the stiffness torque τ of each vertex as a function of displacement φ three times using the same method we used on the individual vertices (see Fig. 11). We calculated the strain energy profile from these measurements (see Fig. 12).

The fingers were driven by a dc motor (Pololu #3080, with #4761 encoder) and a bar-linkage mechanism (see Fig. 13). By controlling the rotation of the dc motor, the rotational motion is translated to a bending motion (input) of the finger's lower two plates through the motor shaft and finger shafts. The finger dimensions (length, width, and α_i) can be found in Table II . M3 screws and nuts were added to some of the faces to change their inertia (see Table III). This ensured that the fingers had the appropriate kinetic energy during each transformation step.

Six extension springs were included in the design to preload the motor-driven linkages and stabilize the system (see Fig. 14). They were 31.75 mm long with a k -value of 49 N/m. Two springs were installed between opposing fingers to pretension the lower vertices, and four were connected between the middle vertices of each finger and the gripper base.

Mechanical stops were included on two hinges of each finger (see Fig. 15). Some potential finger configurations result in nonfunctional grasp modes, and it was simpler to physically prevent these configurations than design our transformation process around avoiding them.

B. Finger Transformation Process

1) Multivertex Transformation: When multiple vertices are transforming simultaneously, the criteria for transformation can change. If one vertex transforms and it shares a spinal crease with another vertex, the transformation criteria for the

TABLE II
FINGER DIMENSIONS

	α_1	α_2	α_3	α_4	α_5	α_6	β	L_0 (mm)	L_1 (mm)	L_2 (mm)	L_3 (mm)	w (mm)
Red finger	40°	65°	60°	40°	55°	55°	45°	50	30	60	50	25
Blue finger	42.5°	65°	40°	60°	55°	55°	45°	50	30	60	50	25

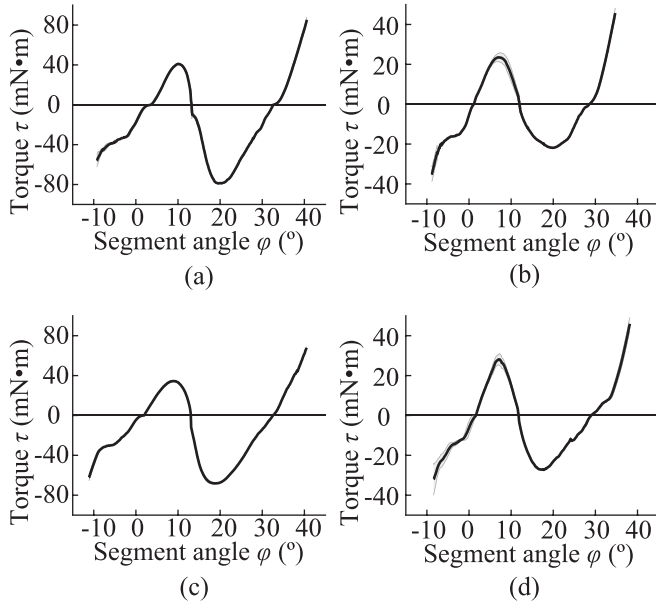


Fig. 11. Stiffness torque τ of finger vertices when $\theta_1 = 12.5^\circ$. (a) Red finger, vertex 1. (b) Red finger, vertex 2. (c) Blue finger, vertex 1. (d) Blue finger, vertex 2. Shaded areas indicate standard deviation, with sample size $N = 3$.

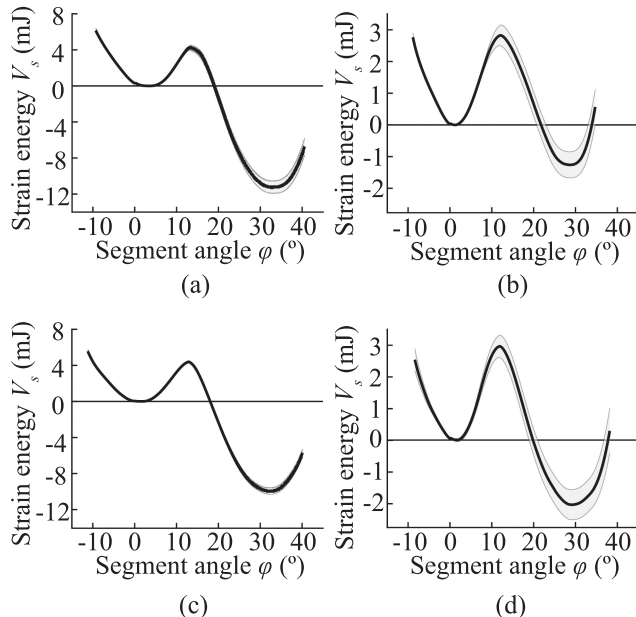


Fig. 12. Finger strain energy V_s when $\theta_1 = 12.5^\circ$. (a) Red finger, vertex 1. (b) Red finger, vertex 2. (c) Blue finger, vertex 1. (d) Blue finger, vertex 2. Shaded areas indicate standard deviation, with sample size $N = 3$.

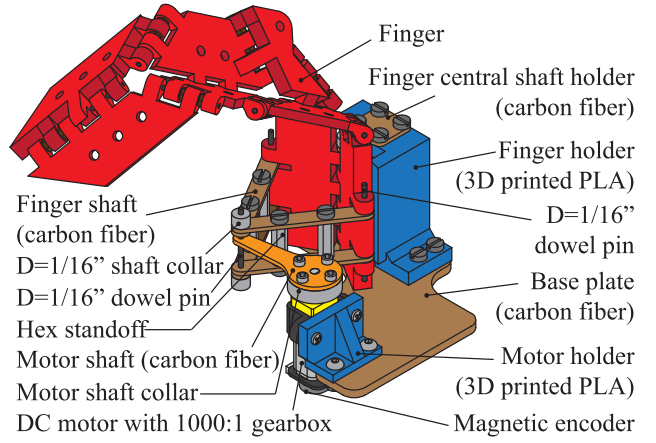


Fig. 13. Finger actuation mechanism.

TABLE III
EXTRA MASS ON FINGERS

Finger	Plate	Added screws			Total mass (g)
		6 mm	8 mm	nut	
Red	1	0	0	0	8.80
	2	0	0	0	7.90
	3	0	0	0	3.28
	4	0	0	0	2.91
	5	2	0	2	4.85
	6	1	0	1	3.37
	7	0	3	3	7.71
	8	3	0	3	5.08
Blue	1	0	0	0	8.71
	2	0	0	0	7.91
	3	0	0	0	2.15
	4	0	0	0	4.69
	5	1	0	2	3.44
	6	2	0	1	4.96
	7	0	3	3	7.71
	8	3	0	3	5.08

follow-on vertex flip: it transforms if $V_t > T$ and it does not transform if $T > V_t$. We refer to this condition as pass-through because the lower spinal crease passes through the flat state. This behavior was previously studied in [33] and can be understood conceptually by the fact that, when the lower spinal crease changes its fold direction (mountain to valley or vice versa), the vertex only transforms if the upper spinal crease does not change direction. Lower kinetic energy is associated with the upper spinal crease remaining folded in its

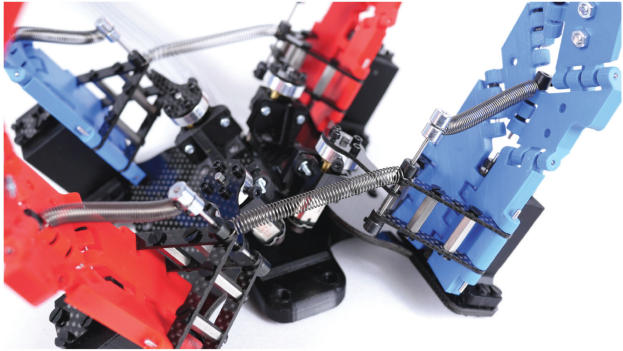


Fig. 14. Six springs are included in the gripper for pretension, including two springs that connect the first segment of opposing fingers and four springs that connect the second segment of each finger to the base.

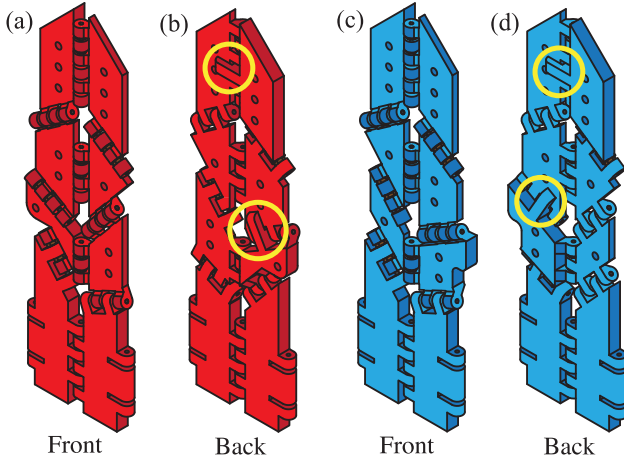


Fig. 15. Finger stops. (a) Red figure design when flat. (b) Back view of the red finger, showing the location of stops (circled). (c) Blue finger design when flat. (d) Back view of the blue finger, showing the location of stops (circled).

original direction, and therefore, lower kinetic energy results in transformation.

In the fingers, we observed this pass-through transformation (or lack of transformation) whenever a lower vertex transformed. Therefore, when considering finger transformation, it may be easier, conceptually, to consider the fold directions of the segments (see Fig. 16). Here, we refer to a segment with the convex side pointing toward the gripper palm as a valley (V) fold, and a segment with the convex side pointing away from the palm as a mountain (M) fold.

2) *Finger Stops:* The mechanical stops prevented their corresponding hinges from folding in one direction (see Fig. 15). One stop was located on the spinal crease of the fourth segment. This kept the fourth segment folded in the mountain direction, which forced the third vertex to be parallel when the third segment was in the mountain direction and antiparallel when the third segment was in the valley direction.

The second stop was on one of the peripheral creases connected to the second vertex. This kept that crease in the mountain direction. When the second segment was in the valley direction, the second vertex was forced into the parallel configuration.

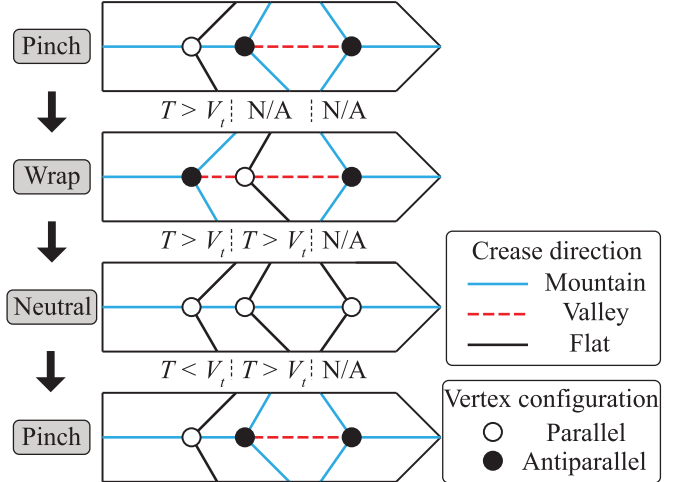


Fig. 16. Crease fold directions during transformation. Because the vertices are connected, the transformation criteria of one vertex depend on its lower neighbor's configuration through the direction of their shared crease.

However, when the second segment was in the mountain direction, the second vertex could enter either configuration because the antiparallel configuration works with the peripheral creases in the mountain direction, and the parallel configuration works when the parallel creases are flat.

3) *Transformation Energy:* We calculated the transformation energy $V_{i,t}$ at each vertex i using a similar model as in Section III-A, including both a strain and gravitational energy component. We calculated the strain energy component $\Delta V_{i,s}$ by measuring the stiffness at each vertex (see Fig. 11) and integrating to calculate the potential energy (see Fig. 12)

$$V_{i,t} = \Delta V_{i,s} + \Delta V_{i,g} \quad (10)$$

$$V_{i,s}(\varphi) = \int_0^\varphi \tau(x)dx \quad (11)$$

$$\Delta V_{i,s} = V_{i,s}(\varphi_u) - V_{i,s}(\varphi_0). \quad (12)$$

The model for the gravitational energy component $\Delta V_{i,g}$ differs slightly because it depends on the weight of all facets connected to the distal side of the vertex, so we present separate sets of equations for each vertex. We first calculated the tilt of each segment relative to the ground (see Fig. 17)

$$\lambda_0 = \xi - \frac{\rho}{2} + \frac{\pi}{2} \quad (13)$$

$$\lambda_{1,0} = \lambda_0 - \varphi_{1,0} \quad (14)$$

$$\lambda_{1,u} = \lambda_0 - \varphi_{1,u} \quad (15)$$

$$\lambda_{2,0} = \lambda_{1,0} - \varphi_{2,0} \quad (16)$$

$$\lambda_{2,u} = \lambda_{1,u} - \varphi_{2,u} \quad (17)$$

$$\lambda_{3,0} = \lambda_{2,0} - \varphi_{3,0} \quad (18)$$

$$\lambda_{3,u} = \lambda_{2,u} - \varphi_{3,u} \quad (19)$$

where φ_x is the displacement of vertex x , λ_j is the tilt angle of segment j with respect to ground, $\lambda_{j,0}$ and $\lambda_{j,u}$ are the tilt angles

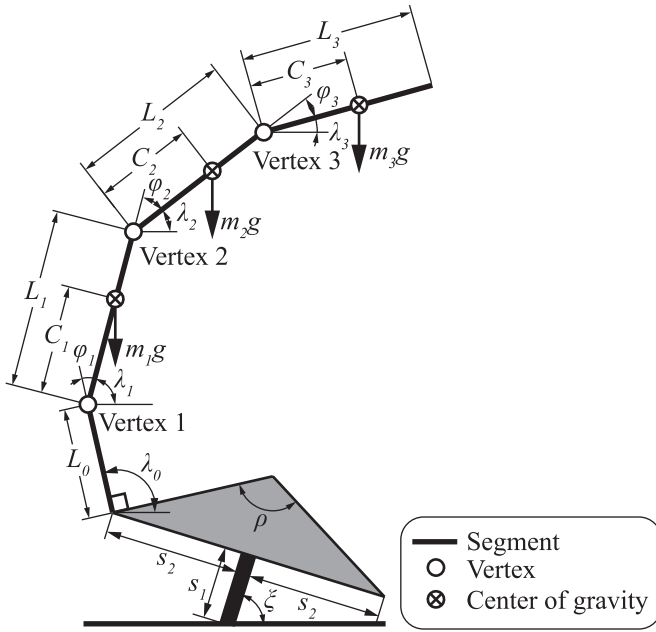


Fig. 17. Linkage model of the finger. λ_j is the tilt angle of segment j with respect to ground. L_j is the length of segment j . m_j is the mass of segment j . C_j is the distance between the center of mass of segment j to vertex j . ρ is the angle between the two sides of fingers ($\rho = 120^\circ$). ξ is the orientation of the UR3e arm's end-effector with respect to ground. s_1 and s_2 are base dimensions. g is the gravitational constant ($j = 0, 1, 2, 3$).

at the initial position and transformation threshold, ρ is the angle deflection at the base of the gripper (in our device, $\rho = 120^\circ$), and ξ is the acute angle between the gripper's central axis and the horizontal plane, which can be calculated from the end-effector speed $\vec{v}_{ee} = [v_x, v_y, v_z]$

$$\xi = \arctan \frac{\sqrt{v_x^2 + v_y^2}}{v_z}. \quad (20)$$

For vertex 1, the gravitational energy $V_{1,g,0}^j$ due to segment j ($j = \{1, 2, 3\}$) before transformation is

$$V_{1,g,0}^1 = m_1 g C_1 \sin \lambda_{1,0} \quad (21)$$

$$V_{1,g,0}^2 = m_2 g (L_1 \sin \lambda_{1,0} + C_2 \sin \lambda_{2,0}) \quad (22)$$

$$V_{1,g,0}^3 = m_3 g (L_1 \sin \lambda_{1,0} + L_2 \sin \lambda_{2,0} + C_3 \sin \lambda_{3,0}). \quad (23)$$

The total gravitational energy is

$$V_{1,g,0} = V_{1,g,0}^1 + V_{1,g,0}^2 + V_{1,g,0}^3. \quad (24)$$

The gravitational energy $V_{1,g,u}^j$ due to segment j at the transformation threshold is

$$V_{1,g,u}^1 = m_1 g C_1 \sin \lambda_{1,u} \quad (25)$$

$$V_{1,g,u}^2 = m_2 g (L_1 \sin \lambda_{1,u} + C_2 \sin \lambda_{2,u}) \quad (26)$$

$$V_{1,g,u}^3 = m_3 g (L_1 \sin \lambda_{1,u} + L_2 \sin \lambda_{2,u} + C_3 \sin \lambda_{3,u}). \quad (27)$$

The total gravitational energy is

$$V_{1,g,u} = V_{1,g,u}^1 + V_{1,g,u}^2 + V_{1,g,u}^3. \quad (28)$$

The potential energy change due to gravity is

$$\Delta V_{1,g} = V_{1,g,u} - V_{1,g,0}. \quad (29)$$

For vertex 2, $V_{2,g,0}^j$ due to segment j ($j = \{2, 3\}$) before transformation is

$$V_{2,g,0}^2 = m_2 g C_2 \sin \lambda_{2,0} \quad (30)$$

$$V_{2,g,0}^3 = m_3 g (L_2 \sin \lambda_{2,0} + C_3 \sin \lambda_{3,0}). \quad (31)$$

The total gravitational energy is

$$V_{2,g,0} = V_{2,g,0}^2 + V_{2,g,0}^3. \quad (32)$$

$V_{2,g,u}^j$ due to segment j at the transformation threshold is

$$V_{2,g,u}^2 = m_2 g C_2 \sin \lambda_{2,u} \quad (33)$$

$$V_{2,g,u}^3 = m_3 g (L_2 \sin \lambda_{2,u} + C_3 \sin \lambda_{3,u}). \quad (34)$$

The total gravitational energy is

$$V_{2,g,u} = V_{2,g,u}^2 + V_{2,g,u}^3. \quad (35)$$

The potential energy change due to gravity is

$$\Delta V_{2,g} = V_{2,g,u} - V_{2,g,0}. \quad (36)$$

Because of the mechanical stop on the fourth segment, the third vertex is always forced into a configuration and was not dynamically modeled.

4) *Kinetic Energy:* For each segment j

$$T_j = \frac{1}{2} m_j v_j^2 = \frac{1}{2} m_j (\omega D_j)^2 = \frac{1}{2} m_j \omega^2 (x_j^2 + y_j^2) \quad (37)$$

$$b_x = s_1 \cos \xi - s_2 \sin \xi \quad (38)$$

$$b_y = s_1 \sin \xi + s_2 \cos \xi \quad (39)$$

$$x_1 = b_x + L_0 \cos \lambda_0 + C_1 \cos \lambda_{1,0} \quad (40)$$

$$y_1 = b_y + L_0 \sin \lambda_0 + C_1 \sin \lambda_{1,0} \quad (41)$$

$$x_2 = b_x + L_0 \cos \lambda_0 + L_1 \cos \lambda_{1,0} + C_2 \cos \lambda_{2,0} \quad (42)$$

$$y_2 = b_y + L_0 \sin \lambda_0 + L_1 \sin \lambda_{1,0} + C_2 \sin \lambda_{2,0} \quad (43)$$

$$x_3 = b_x + L_0 \cos \lambda_0 + L_1 \cos \lambda_{1,0} + L_2 \cos \lambda_{2,0} + C_3 \cos \lambda_{3,0} \quad (44)$$

$$y_3 = b_y + L_0 \sin \lambda_0 + L_1 \sin \lambda_{1,0} + L_2 \sin \lambda_{2,0} + C_3 \sin \lambda_{3,0} \quad (45)$$

where m_j is the weight of each segment, v_j is the linear velocity at the center of gravity, ω is the angular velocity of the segment, D_j is the distance between the center of mass and the rotational center, x_j and y_j are local coordinates of the center of mass, and s_1 and s_2 are base dimensions (see Fig. 17).

To predict the transformation of vertex 1, we include the kinetic energy of all three segments

$$T = T_1 + T_2 + T_3. \quad (46)$$

To predict the transformation of vertex 2, we include the kinetic energy of segments 2 and 3

$$T = T_2 + T_3. \quad (47)$$

TABLE IV
RED FINGER TRANSFORMATION MODELING

Red finger		Vertex 1		Vertex 2		Vertex 3	
		Kinetic	Transformation	Kinetic	Transformation	Kinetic	Transformation
Pinch to wrap	Criteria	$T > V_t$		N/A		N/A	
	Energy (mJ)	2.9354	2.1076	—	—	—	—
Wrap to neutral	Criteria	$T > V_t$		$T > V_t$		N/A	
	Energy (mJ)	2.1915	2.1033	1.9525	-3.8480	—	—
Neutral to pinch	Criteria	$T < V_t$		$T > V_t$		N/A	
	Energy (mJ)	3.6146	3.7469	3.1657	2.3487	—	—

TABLE V
BLUE FINGER TRANSFORMATION MODELING

Red finger		Vertex 1		Vertex 2		Vertex 3	
		Kinetic	Transformation	Kinetic	Transformation	Kinetic	Transformation
Pinch to wrap	Criteria	$T > V_t$		N/A		N/A	
	Energy (mJ)	2.9812	1.8008	—	—	—	—
Wrap to neutral	Criteria	$T > V_t$		$T > V_t$		N/A	
	Energy (mJ)	2.2386	1.8385	1.9788	-3.1143	—	—
Neutral to pinch	Criteria	$T < V_t$		$T > V_t$		N/A	
	Energy (mJ)	3.6658	3.7910	3.1797	2.3766	—	—

5) *Pinch to Wrap Mode:* In the pinch mode, the configurations of vertices 1–3 were parallel, antiparallel, and antiparallel, respectively. The fold direction of the segments were, in order, M-M-V-M. In wrap mode, the vertices were antiparallel, parallel, antiparallel, and the segment fold directions were M-V-V-M. In each finger, the stops (see Fig. 15) forced the third and fourth segments to maintain their fold direction, so only the second segment (the upper segment of the first vertex) needs to be considered (see Fig. 16).

6) *Wrap to Neutral Mode:* In the wrap mode, the vertex configurations were antiparallel, parallel, antiparallel, and the segment fold directions were M-V-V-M. In the neutral configuration, the vertex configurations were all parallel, and the segment fold directions all mountain. Therefore, the second and third segments had to change direction, while the stop on the fourth segment forced it to maintain the mountain direction. The second and third segments depended on the dynamics at the first and second vertices, respectively. To transform successfully, the kinetic energy of plates 3–8 had to be greater than the transformation energy of vertex 1 and the kinetic energy of plates 5–8 had to be greater than the transformation energy of vertex 2 (see Fig. 16).

7) *Neutral to Pinch Mode:* In the neutral mode, all vertices were parallel, and the segment fold directions were M-M-M-M. In the pinch mode, the vertex configurations were parallel, antiparallel, and antiparallel, and the segment fold directions were M-M-V-M. Therefore, only the third segment changed direction, and only the second vertex transformed. To perform this transformation successfully, the kinetic energy of plates 3–8 had to be less than the transformation energy of vertex 1, but the kinetic energy of plates 5–8 had to be greater than the transformation energy of vertex 2 (see Fig. 16).

C. Gripper Transformation Process

In each transformation step, the transforming fingers were set to an input $\theta_1 = 12.5^\circ$ and the nontransforming fingers were set to $\theta_1 = 55^\circ$. The gripper was oriented so that the transforming fingers were accelerated inward. The kinetic and potential energies of the vertices at each transformation step can be found in Tables IV and V.

1) *Pinch to Wrap Mode:* This transformation occurred in two steps, and each step transformed two fingers. The gripper reached a velocity of 0.98 m/s before being stopped by the arm. This velocity was calculated so that the kinetic energy of the plates above vertex 1 was enough to overcome the vertex's bistable point (see Tables IV and V, Supplemental Dataset S2).

2) *Wrap to Forklift Mode:* This transformation occurred in three steps, and each step transformed two fingers. In the first step, the fingers transformed from a wrap to a neutral configuration. The gripper reached a velocity of 0.95 m/s before stopping, sufficient for the kinetic energy of the plates above vertex 1 to be greater than the transformation energy of vertex 1 (see Tables IV and V, Dataset S2).

In the second step, the same two fingers transformed from a neutral to a pinch mode. To achieve this transformation, the gripper was accelerated to a speed of 0.30 m/s. At this speed, the kinetic energy of the plates above vertex 1 was less than amount necessary to trigger vertex transformation. The kinetic energy of the plates above vertex 2 was sufficient to trigger transformation of vertex 2 (see Tables IV and V, Dataset S2).

In the third step, the other two fingers transformed from a wrap to a neutral position, using the same steps as the first step. The calculations for these transformations can be found in Tables IV and V, Dataset S2.

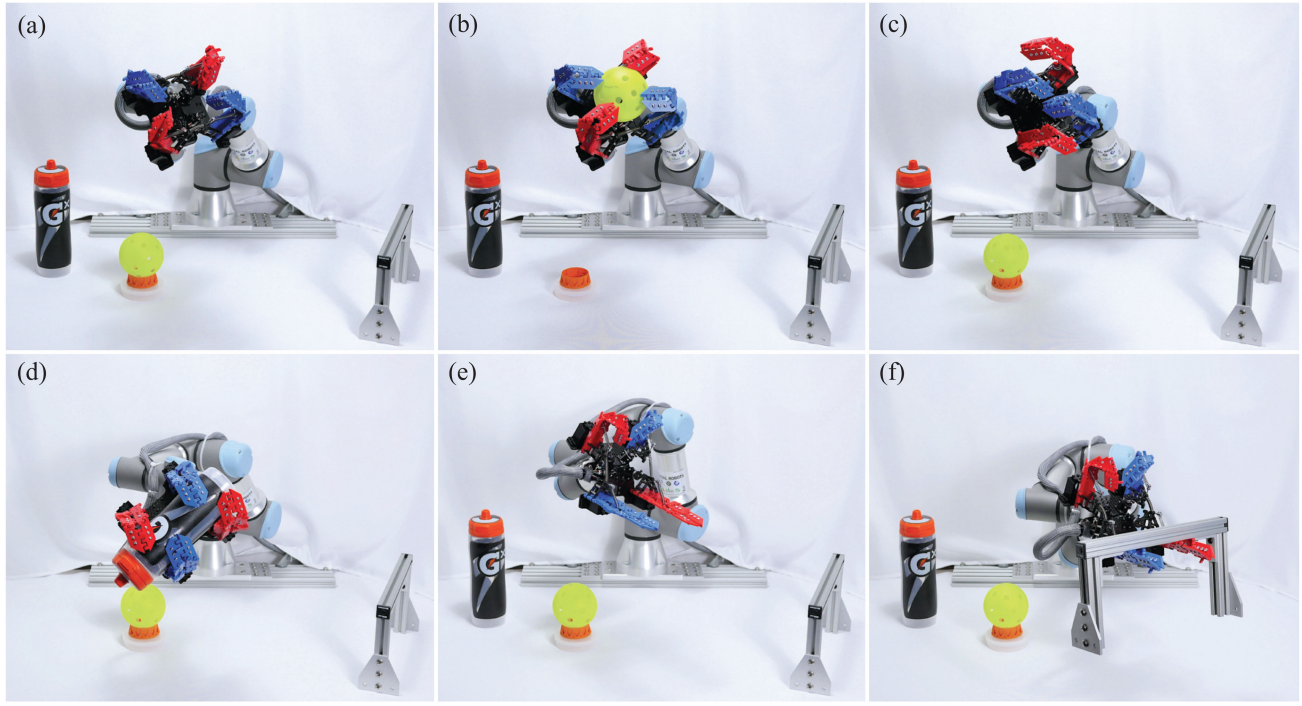


Fig. 18. Demonstration of the transforming gripper performing three different grasps. (a) Gripper starts in a radial pinch mode. (b) It pinches a ball. (c) It transforms into a cylindrical wrap mode. (d) It grasps a water bottle. (e) It transforms again into a forklift mode. (f) It lifts a metal beam.

3) *Forklift to Pinch Mode*: This transformation occurred in one step, transforming two fingers from the neutral to the pinch configuration. To achieve this transformation, vertices 2 and 3 had to transform, so the gripper was accelerated to a speed of 0.30 m/s, similar to the second step of the previous transformation (see Tables IV and V, Dataset S2).

D. Gripper Demonstration

To demonstrate that the gripper could apply these grasps and transform between them, the gripper was mounted to the final joint of a Universal Robots UR3e robotic arm with a preprogrammed trajectory that included six phases: three grasp phases in which the arm positioned the gripper to engage three different objects (a plastic ball, 41 g; a water bottle, 155 g; and an aluminum beam structure, 642 g), and three transformation phases in which the gripper reconfigured from a pinch to wrap mode, wrap to forklift mode, and forklift to pinch mode, demonstrating that the transformation is reversible and repeatable (Supplemental Video S1).

The fingers were controlled by two RoMeo v2 microcontrollers; each board controlled a pair of motors. The gripper was controlled by a push button connected to the microcontrollers; upon pressing, the robot would perform a single step of the demonstration and then halt until the next button press.

Gripper transformation consisted of multiple flicks, separated by rotation of the gripper. During each flick, two of the fingers folded to $\theta_1 = 55^\circ$ to lock them in place, and the other two opened to $\theta_1 = 12.5^\circ$, which made them susceptible to reconfiguration. A specific impulse, based on the earlier vertex

characterization, was applied to the gripper by accelerating and rapidly decelerating the arm, inducing some of the vertices to snap through (see Fig. 16 and Tables IV and V). The relevant energy calculations for each transformation can be found in the Supplemental Dataset S2.

In the first phase [see Fig. 18(a)], the gripper grasped a plastic wiffle ball with a pinch grasp. This mode required the first and third vertices to be antiparallel, so that all fingers bend inward to pinch at a point [see Fig. 18(b)]. After lifting and replacing the ball, it then transformed, reconfiguring the first vertex to parallel and the second vertex to antiparallel [see Fig. 18(c)]. In this configuration, the fingers on either side spiraled in opposite directions to wrap around cylindrical objects. The gripper then grasped, lifted, and put back a water bottle [see Fig. 18(d)]. The gripper transformed again, reconfiguring two of its fingers so that all vertices were parallel [see Fig. 18(e)]. In this configuration, it lifted an aluminum bar from below before putting it back [see Fig. 18(f)]. Finally, the gripper transformed back to the pinch mode and completed its demonstration. The sequence was repeated ten times, and each time all transformations and grasps were performed successfully. Transformation of individual fingers took between 0.14 and 0.35 s (see Table VI).

The velocity and acceleration of the robot arm during the demonstration were predefined and based on a series of positioning waypoints (Supplemental Dataset S3). Each joint began from rest and reached a final target velocity through a constant acceleration. During the transformation phases, the target velocities were chosen so that the gripper reached the linear velocity and orientation necessary for transformation. The velocity of each joint at the end position and the moving time during the

TABLE VI
FINGER TRANSFORMATION DURATION

Transformation type	Transformation duration (s)
Pinch to wrap	0.35
Wrap to neutral	0.21
Neutral to pinch	0.14

fingers' mode transformations can be found in the Supplemental Dataset S4.

V. DISCUSSION

These results indicate that dynamic origami transformation can be used in load-bearing machines. By using elements with nonlinear stiffness, the origami structure is capable of both the compliance for transformation and the stiffness to interact with the environment. In conjunction with the origami string template, we can combine a wide range of potential kinematic behaviors in a single mechanism and reconfigure between them. By using this transformation in a robotic gripper, we show that the technology is capable of the practical kinematics necessary for intelligent machines and the ability to transform under a variety of orientations.

There are technical limitations to the size and stiffness of dynamically transforming origami machines. We expect that as an origami machine gets larger, its mass will grow faster than its stiffness due to the square-cube law. In addition, when multiple vertices are arranged in series, the backlash at each successive vertex compounds so that patterns with more vertices will be more compliant. With our current design and actuation, we observed that origami strings with more than four vertices were practically uncontrollable due to this compounding behavior. We expect that this backlash-dependent compliance can be minimized through a combination of more precise fabrication and better controllers; if the system has a sufficiently precise torque input, it can reliably induce reconfiguration within an arbitrarily small backlash window and less backlash is necessary at each vertex.

There may also be challenges to scaling these systems down in size. Origami lends itself to millimeter-scale fabrication, but the stiffness would still need to be precisely tuned for transformation, which may be more difficult with planar fabrication techniques. We would also expect to need faster inputs to compensate for the reduced mass when balancing the kinetic and transformation energies.

There are also design challenges in the individual creases. Because our faces have nonzero thicknesses and no offset, the maximum fold angle is limited to 55°. Previous work has shown how to account for facet thickness [7], [40], and such designs could be integrated with transforming systems.

This article focuses on a relatively simple origami template, but we believe this approach to origami transformation could be applied to arbitrarily complex patterns. The transformation of vertices with five or more edges would be more challenging both because there are more degrees of freedom and more stable configurations, but we expect that the extra degrees of freedom

could be modeled with additional state variables, and there is a known upper bound on the number of possible configurations for a given vertex [41].

More complex vertex networks could also be transformed, but would likely require a more sophisticated model. Our current model assumes a fixed transformation threshold for each vertex, which is an acceptable assumption for the relatively small number of vertices in this design. However, the actual threshold moves slightly as the mechanism moves, and each vertex may approach this threshold at a different point in time, requiring a more complex set of equations to accurately capture the system state. We expect that the most substantial limit to complexity is in the compliance of the overall structure and precision in the controls, since the transformation of a single vertex is coupled to every other vertex in the system.

There are many examples of nonorigami multigrasp grippers, but we believe that this gripper demonstrates the potential to outperform them in some ways. Some existing grippers use multiple actuated degrees of freedom to effect different grasping modes [42]–[44]. Others have a single actuator and passively adapt to physical constraints [45], [46]. The origami gripper presented in this article has the strength of both approaches by allowing for multiple kinematically constrained grasping modes, all driven by a single actuator. It also allows the designer to harness the theoretical complexity and computational tools of origami to quickly realize complex shapes and behaviors. The most substantial downside is that this gripper, like many other origami machines, is substantially more compliant. While it can lift some objects, it does not have the payload capacity of other similarly sized grippers [42].

REFERENCES

- [1] J. P. Whitney, P. S. Sreetharan, K. Y. Ma, and R. J. Wood, "Pop-up book MEMS," *J. Micromech. Microeng.*, vol. 21, no. 11, 2011, Art. no. 115021.
- [2] M. Z. Miskin *et al.*, "Graphene-based bimorphs for micron-sized, autonomous origami machines," *Proc. Nat. Acad. Sci.*, vol. 115, no. 3, pp. 466–470, 2018.
- [3] X. Liu, S. Yao, S. V. Georgakopoulos, B. S. Cook, and M. M. Tentzeris, "Reconfigurable helical antenna based on an origami structure for wireless communication system," in *Proc. IEEE MTT-S Int. Microw. Symp.*, 2014, pp. 1–4.
- [4] S. I. H. Shah, M. M. Tentzeris, and S. Lim, "Low-cost circularly polarized origami antenna," *IEEE Antennas Wireless Propag. Lett.*, vol. 16, pp. 2026–2029, 2017.
- [5] Y. Nishiyama, "Miura folding: Applying origami to space exploration," *Int. J. Pure Appl. Math.*, vol. 79, no. 2, pp. 269–279, 2012.
- [6] L. Wilson, S. Pellegrino, and R. Danner, "Origami sunshield concepts for space telescopes," in *Proc. 54th AIAA/ASME/ASCE/AHS/ASC Struct., Struct. Dyn., Mater. Conf.*, 2013, Art. no. 1594.
- [7] S. A. Zirbel *et al.*, "Accommodating thickness in origami-based deployable arrays," *J. Mech. Des.*, vol. 135, no. 11, 2013, Art. no. 111005.
- [8] C. D. Onal, M. T. Tolley, R. J. Wood, and D. Rus, "Origami-inspired printed robots," *IEEE/ASME Trans. Mechatronics*, vol. 20, no. 5, pp. 2214–2221, Oct. 2015.
- [9] A. Firouzeh and J. Paik, "An under-actuated origami gripper with adjustable stiffness joints for multiple grasp modes," *Smart Mater. Struct.*, vol. 26, no. 5, 2017, Art. no. 055035.
- [10] D. Jeong and K. Lee, "Design and analysis of an origami-based three-finger manipulator," *Robotica*, vol. 36, no. 2, pp. 261–274, 2018.
- [11] W. P. Weston-Dawkes, A. C. Ong, M. R. A. Majit, F. Joseph, and M. T. Tolley, "Towards rapid mechanical customization of cm-scale self-folding agents," in *Proc. IEEE/RSJ Int. Conf. Intell. Robots Syst.*, 2017, pp. 4312–4318.

- [12] C. Liu, A. Orlofsky, C. D. Kitcher, and S. M. Felton, "A self-folding pneumatic piston for mechanically robust origami robots," *IEEE Robot. Autom. Lett.*, vol. 4, no. 2, pp. 1372–1378, Apr. 2019.
- [13] E. Hawkes *et al.*, "Programmable matter by folding," *Proc. Nat. Acad. Sci.*, vol. 107, no. 28, pp. 12 441–12445, 2010.
- [14] S. Miyashita, S. Guitron, S. Li, and D. Rus, "Robotic metamorphosis by origami exoskeletons," *Sci. Robot.*, vol. 2, no. 10, 2017, Art. no. eaao4369.
- [15] C. D. Santangelo, "Extreme mechanics: Self-folding origami," *Annu. Rev. Condens. Matter Phys.*, vol. 8, pp. 165–183, 2017.
- [16] T. S. Shim, S.-H. Kim, C.-J. Heo, H. C. Jeon, and S.-M. Yang, "Controlled origami folding of hydrogel bilayers with sustained reversibility for robust microcarriers," *Angewandte Chemie Int. Ed.*, vol. 51, no. 6, pp. 1420–1423, 2012.
- [17] M. Jamal *et al.*, "Bio-origami hydrogel scaffolds composed of photocrosslinked PEG bilayers," *Adv. Healthcare Mater.*, vol. 2, no. 8, pp. 1142–1150, 2013.
- [18] C. M. Gomes, C. Liu, J. A. Paten, S. M. Felton, and L. F. Deravi, "Protein-based hydrogels that actuate self-folding systems," *Adv. Funct. Mater.*, vol. 29, no. 4, 2019, Art. no. 1805777.
- [19] G. Li, G. Fei, H. Xia, J. Han, and Y. Zhao, "Spatial and temporal control of shape memory polymers and simultaneous drug release using high intensity focused ultrasound," *J. Mater. Chem.*, vol. 22, no. 16, pp. 7692–7696, 2012.
- [20] A. Firouzeh and J. Paik, "Robogami: A fully integrated low-profile robotic origami," *J. Mech. Robot.*, vol. 7, no. 2, 2015, Art. no. 021009.
- [21] Y. W. Yi and C. Liu, "Magnetic actuation of hinged microstructures," *J. Microelectromech. Syst.*, vol. 8, no. 1, pp. 10–17, 1999.
- [22] S.-J. Kim, D.-Y. Lee, G.-P. Jung, and K.-J. Cho, "An origami-inspired, self-locking robotic arm that can be folded flat," *Sci. Robot.*, vol. 3, no. 16, 2018, Art. no. eaar 2915.
- [23] J. A. Faber, A. F. Arrieta, and A. R. Stuwart, "Bioinspired spring origami," *Science*, vol. 359, no. 6382, pp. 1386–1391, 2018.
- [24] M. E. Hossain Bhuiyan, D. Semer, and B. P. Trease, "Dynamic modeling and analysis of strain energy and centrifugal force deployment of an origami flasher," in *Proc. Int. Des. Eng. Tech. Conf./Comput. Inf. Eng. Conf.*, 2017, Art. no. V0 5BT08A063.
- [25] K. E. Laflin, C. J. Morris, T. Muqeem, and D. H. Gracias, "Laser triggered sequential folding of microstructures," *Appl. Phys. Lett.*, vol. 101, no. 13, 2012, Art. no. 131901.
- [26] M. E. Nisser, S. M. Felton, M. T. Tolley, M. Rubenstein, and R. J. Wood, "Feedback-controlled self-folding of autonomous robot collectives," in *Proc. IEEE/RSJ Int. Conf. Intell. Robots Syst.*, 2016, pp. 1254–1261.
- [27] S. Felton, M. Tolley, E. Demaine, D. Rus, and R. Wood, "A method for building self-folding machines," *Science*, vol. 345, no. 6197, pp. 644–646, 2014.
- [28] X. Sun, S. M. Felton, R. Niifyama, R. J. Wood, and S. Kim, "Self-folding and self-actuating robots: A pneumatic approach," in *Proc. IEEE Int. Conf. Robot. Autom.*, 2015, pp. 3160–3165.
- [29] S. M. Felton, "Methods for building self-folding machines," doctoral dissertation, Graduate School Arts Sci., Harvard Univ., Cambridge, MA, USA, 2015.
- [30] B. G.-g. Chen and C. D. Santangelo, "Branches of triangulated origami near the unfolded state," *Phys. Rev. X*, vol. 8, no. 1, 2018, Art. no. 011034.
- [31] T. Tachi and T. C. Hull, "Self-foldability of rigid origami," *J. Mech. Robot.*, vol. 9, no. 2, 2017, Art. no. 021008.
- [32] Y. Chen, J. Yan, and J. Feng, "Geometric and kinematic analyses and novel characteristics of origami-inspired structures," *Symmetry*, vol. 11, no. 9, 2019, Art. no. 1101.
- [33] C. Liu and S. M. Felton, "Transformation dynamics in origami," *Phys. Rev. Lett.*, vol. 121, no. 25, 2018, Art. no. 254101.
- [34] F. Zuliani, C. Liu, J. Paik, and S. M. Felton, "Minimally actuated transformation of origami machines," *IEEE Robot. Autom. Lett.*, vol. 3, no. 3, pp. 1426–1433, Jul. 2018.
- [35] C. Liu, Z. M. H. Aung, and S. M. Felton, "Dynamic transformation of an origami string using a stacked-Miura cell," in *Proc. Int. Des. Eng. Tech. Conf./Comput. Inf. Eng. Conf.*, 2019, Art. no. V0 5BT07A031.
- [36] S. Kamrava, D. Mousanezhad, S. M. Felton, and A. Vaziri, "Programmable origami strings," *Adv. Mater. Technol.*, vol. 3, no. 3, 2018, Art. no. 1700276.
- [37] S. Kamrava, R. Ghosh, Y. Yang, and A. Vaziri, "Slender origami with complex 3D folding shapes," *Europhys. Lett.*, vol. 124, no. 5, 2018, Art. no. 58001.
- [38] S. Kamrava, C. Liu, A. Q. Orlofsky, A. Vaziri, and S. M. Felton, "A closed-form solution for the kinematics of asymmetric Miura vertices," 2020, *arXiv:2001.07657*.
- [39] A. Orlofsky, C. Liu, S. Kamrava, A. Vaziri, and S. M. Felton, "Mechanically programmed miniature origami grippers," in *Proc. IEEE Int. Conf. Robot. Autom.*, 2020, pp. 2872–2878.
- [40] R. J. Lang, N. Brown, B. Ignaut, S. Magleby, and L. Howell, "Rigidly foldable thick origami using designed-offset linkages," *J. Mech. Robot.*, vol. 12, no. 2, 2020, Art. no. 021106.
- [41] Z. Abel *et al.*, "Rigid origami vertices: Conditions and forcing sets," *J. Comput. Geometry*, vol. 7, no. 1, pp. 171–184, 2016.
- [42] C. Canali *et al.*, "High reconfigurable robotic gripper for flexible assembly," in *Proc. Int. Des. Eng. Tech. Conf./Comput. Inf. Eng. Conf.*, 2014, Art. no. V0 5BT08A019.
- [43] Z. Xu and E. Todorov, "Design of a highly biomimetic anthropomorphic robotic hand towards artificial limb regeneration," in *Proc. IEEE Int. Conf. Robot. Autom.*, 2016, pp. 3485–3492.
- [44] H. Nakamoto, M. Ohtake, K. Komoda, A. Sugahara, and A. Ogawa, "A gripper system for robustly picking various objects placed densely by suction and pinching," in *Proc. IEEE/RSJ Int. Conf. Intell. Robots Syst.*, 2018, pp. 6093–6098.
- [45] M. Manti, T. Hassan, G. Passetti, N. D'Elia, C. Laschi, and M. Cianchetti, "A bioinspired soft robotic gripper for adaptable and effective grasping," *Soft Robot.*, vol. 2, no. 3, pp. 107–116, 2015.
- [46] T. Nishimura, K. Mizushima, Y. Suzuki, T. Tsuji, and T. Watanabe, "Variable-grasping-mode underactuated soft gripper with environmental contact-based operation," *IEEE Robot. Autom. Lett.*, vol. 2, no. 2, pp. 1164–1171, Apr. 2017.



Chang Liu received the B.S. degree in mechanical engineering from the Harbin Institute of Technology, Harbin, China, in 2014, the M.S. degree in mechanical engineering from Northwestern University, Evanston, IL, USA, in 2016, and the Ph.D. degree in mechanical engineering from Northeastern University, Boston, MA, USA, 2020.

He was a part of an exchange program with the University of California at Riverside, Riverside, CA, USA, from 2013 to 2014. He is currently a Postdoctoral Researcher with the University of California at Los Angeles, Los Angeles, CA, USA.



Sam J. Wohlever is currently working toward the B.S. degree in mechanical engineering with Northeastern University, Boston, MA, USA.

His current work focuses on mechanically and thermally modeling composite systems aligned through novel means. His research interests include composite networks and metamaterials, especially their application to origami robotics.



María B. Ou is working toward the B.S. degree in mechanical engineering and a minor in robotics with Northeastern University, Boston, MA, USA.

Her research interests include novel design, actuation, sensing, and controls for mechatronics applications.



Taskin Padir received the B.S. degree in electrical and electronics engineering from Middle East Technical University, Ankara, Turkey, in 1993, and the M.S. and Ph.D. degrees in electrical and computer engineering from Purdue University, West Lafayette, IN, USA, in 1997 and 2004 respectively.

He is currently an Associate Professor with the Department of Electrical and Computer Engineering, Northeastern University, Boston, MA, USA. He is the Director of Robotics and Intelligent Vehicles Research Laboratory. He is also the Founding Director of the Institute for Experiential Robotics, Northeastern University. His research interests include supervised autonomy for humanoid robots, shared autonomy for intelligent vehicles, and human-in-the-loop control systems.



Samuel M. Felton received the B.S. degree in mechanical engineering and the M.Eng. degree in bioengineering from the Massachusetts Institute of Technology, Cambridge, MA, USA, in 2007, and the Ph.D. degree in engineering sciences from Harvard University, Cambridge, in 2015.

From 2016 to 2019, he was an Assistant Professor with Northeastern University, Boston, MA, where he directed the Expeditionary Robotics Laboratory. His research interests include origami engineering and transformable robots.